(Received 2 April 2026, Accepted 29 April 2026, Scheduled 17 May 2026)

Design and Analysis of a Variable-Flux Permanent Magnet Synchronous Motor Based on a Hybrid Series-Parallel Permanent Magnet System

Zhongan Yu, Long Chen*, Faneng Wu, Qianli Jia, and Fangrong Wang

School of Electrical Engineering and Automation, Jiangxi University of Science and Technology, Ganzhou 341000, Jiangxi, China

ABSTRACT: To address the shortcomings of conventional permanent magnet synchronous motors (CPMSMs), such as the inability to adjust the permanent magnet field and a narrow speed control range, this paper proposes a variable leakage flux permanent magnet synchronous motor (HPM-VLFM) based on a hybrid series-parallel permanent magnet configuration. This motor achieves a variable leakage flux permanent magnet motor (VLFM) by designing a magnetic barrier on the q-axis, and further realizes the HPM-VLFM by designing ferrite permanent magnets with a series-parallel magnetic circuit. First, this paper introduces a rotor topology of the proposed motor and establishes its equivalent magnetic circuit to elucidate its operating principle. Second, sensitivity analysis and response surface analysis are employed to investigate the relationship between parameters and response variables, and an optimal solution is obtained based on the given constraints. Finally, based on two-dimensional finite element analysis (FEA), the electromagnetic characteristics of the proposed motor were analyzed in detail, including variable flux leakage characteristics, no-load characteristics, inductance characteristics, and torque efficiency characteristics. The results indicate that the HPM-VLFM has a wider speed control range and higher efficiency than VLFM.

1. INTRODUCTION

Permanent magnet synchronous motors (PMSMs) are widely used in electric vehicle traction motors due to their high efficiency, high output torque, high power density, and excellent dynamic performance [1, 2]. However, because the permanent magnetic field of the PMSM rotor is fixed, increasing torque density typically requires applying a large direct-axis demagnetizing current to generate reluctance torque. This leads to increased losses and reduced efficiency, resulting in certain limitations in speed control for conventional PMSMs and making them unsuitable for high-speed drive applications [3, 4].

Currently, unlike traditional PMSMs that rely on direct-axis demagnetizing currents or hybrid excitation windings to adjust the magnetic field, Variable Leakage-Flux Permanent Magnet Motors (VLFMs) regulate the air-gap flux by altering the saturation level of the rotor's leakage flux path. This makes them suitable for applications requiring wide speed regulation and high reliability, such as in electric vehicle traction systems [5, 6]. Ref. [7] investigated the flux barrier topology for regulating VLFMs from the perspective of harmonic components in air-gap flux density. By appropriately configuring the flux barrier of the VLFM, the power factor was improved by 35% under rated conditions, while maintaining a wide speed range. Refs. [8] and [9] conducted a comprehensive analysis and evaluation of VLFM topologies. As the ratio of magnetic resistance torque in VLFMs increases, the risk of load demagnetization also increases. Therefore, during the design phase, the trajectory of NdFeB permanent magnets should be evaluated when demagnetizing currents are applied to avoid local irreversible demagnetization. Ref. [10] proposed a series hybrid permanent magnet variable flux motor using a combination of low-coercivity and high-coercivity permanent magnets. The proposed motor features a wide range of magnetization states, low magnetization and demagnetization currents, and a low risk of demagnetization.

Although VLFM can regulate the air-gap flux, the configuration of a magnetic bridge on the stator axis and an air-gap magnetic barrier on the rotor axis increases the magnetic circuit resistance and reduces the effective air-gap flux, resulting in a decrease in VLFM torque [11, 12]. Therefore, it is necessary to explore methods to enhance VLFM torque.

To increase the torque of PMSMs, many researchers have employed blends of different permanent magnet materials to form distinct magnetic circuits and enhance torque [13]. Ref. [14] embedded ferrite in the rotor slots to replace part of the heavy-rare-earth permanent magnet material, achieving greater magnetic resistance torque and enhancing the ferrite's resistance to demagnetization. Ref. [15] modeled a parallel configuration of ferrite and NdFeB magnetic circuits, thereby improving the utilization of the NdFeB permanent magnets. Refs. [16] and [17] proposed a series-parallel permanent magnet motor with an asymmetric magnet structure. By employing a special asymmetric rotor topology, they improve the utilization of permanent magnets and reduce superposition and coupling losses in the permanent magnet torque.

* Corresponding author: Long Chen (18370031053@163.com).

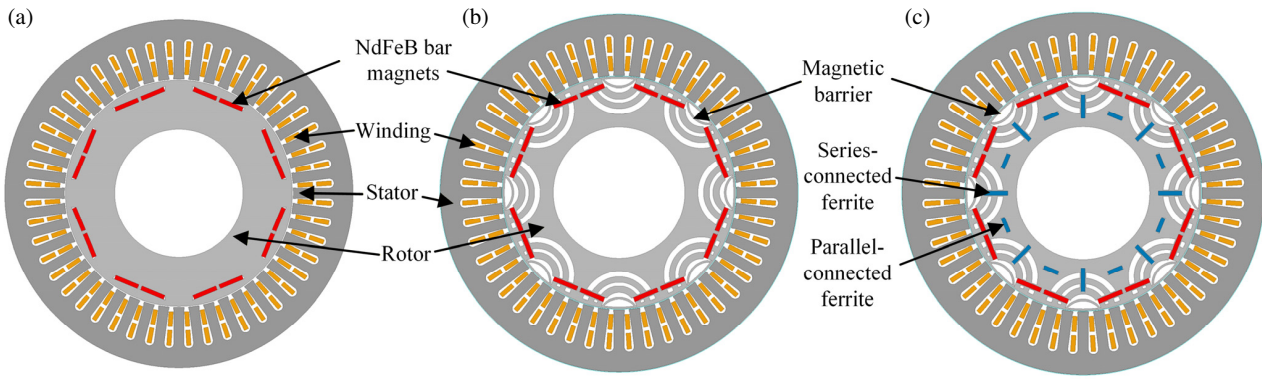

FIGURE 1. Motor topologies: (a) CPMSM. (b) VLFM. (c) HPM-VLFM.

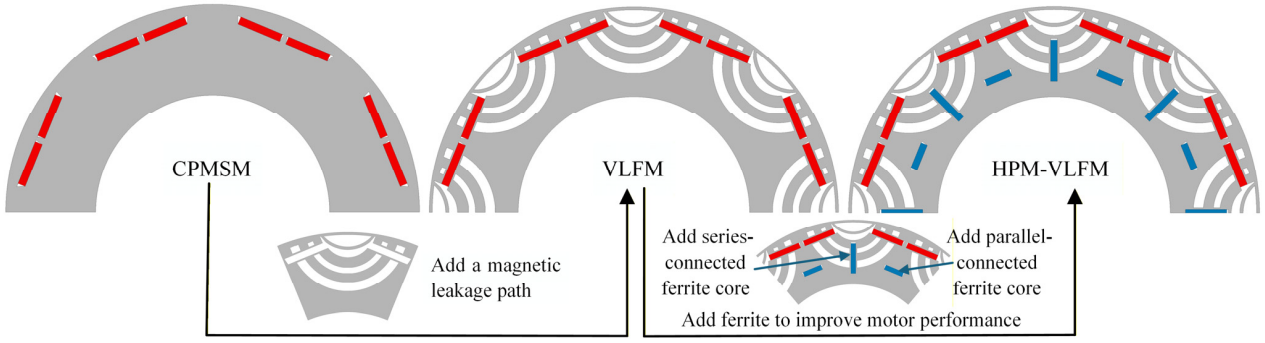

FIGURE 2. The rotor structure of CPMSM evolves step by step to VLFM and HPM-VLFM rotor structure.

This paper investigates and designs a variable-flux-magnet permanent magnet synchronous motor with a hybrid permanent magnet structure (HPM-VLFM) and conducts performance analysis. While broadening the speed range, this motor also enhances the output torque to a certain extent by designing a series-parallel magnetic circuit composed of ferrite and NdFeB permanent magnets. The main contributions of this paper can be summarized as follows:

1) A novel VLFM is proposed, and its operating principle is elucidated through equivalent magnetic circuit analysis.

2) Based on the novel VLFM, a series-parallel hybrid permanent magnet VLFM is further proposed. By establishing and analyzing the magnetic circuit, the mechanism by which series-connected and parallel-connected ferrite magnets enhance output torque is systematically elucidated.

3) A genetic algorithm optimization method for enhancing the output torque of the series-parallel hybrid permanent magnet VLFM was developed and validated. This method combines finite element (FE) modeling with two-dimensional equivalent magnetic circuit modeling to optimize the series-parallel ferrite configuration and variable leakage flux barrier structures, thereby achieving an increase in motor output torque.

The structure of this paper is as follows. Section 2 discusses the shortcomings of traditional bar-type PMSMs and VLFMs, and based on this, proposes a series-parallel hybrid permanent magnet VLFM; simultaneously, equivalent magnetic circuit models for the three motors are established to elucidate their operating principles. Section 3 conducts multi-objective optimization for the series-parallel hybrid permanent magnet VLFM topology and compares its performance in other aspects while enhancing the motor's output torque. Section 4 verifies the reliability of the proposed motor through finite element analysis. Section 5 summarizes the entire paper.

2. MOTOR TOPOLOGY AND OPERATING PRINCIPLE

2.1. Motor Topology

Based on the conventional bar-type permanent magnet synchronous motor (CPMSM), this paper designs a variable-flux permanent magnet motor (VLFM) with a rotor incorporating bar-type neodymium-iron-boron permanent magnets. To enhance the output torque of the VLFM, a hybrid permanent magnet variable-flux permanent magnet synchronous motor (HPM-VLFM) is further developed by designing ferrite permanent magnets in a series-parallel magnetic circuit, as shown in Figure 1. The stator winding structures of all three motors are identical, featuring an 8-pole, 48-slot design; the only difference lies in the rotor structure. Figure 2 illustrates the step-by-step evolution of the rotor structure from the CPMSM to the VLFM and HPM-VLFM.

First, because CPMSMs have a relatively large leakage flux path, arc-shaped and semicircular magnetic barriers are incorporated into the q-axis magnetic circuit of the CPMSM to create two leakage flux paths, resulting in a VLFM. The leakage magnetic paths of the VLFM block the downstream q-axis pathway, thereby reducing the self-leakage flux of the NdFeB permanent magnets; simultaneously, this design reduces the q-axis inductance (L_q) and provides a pathway for leakage flux variations under different operating conditions. Second, to increase

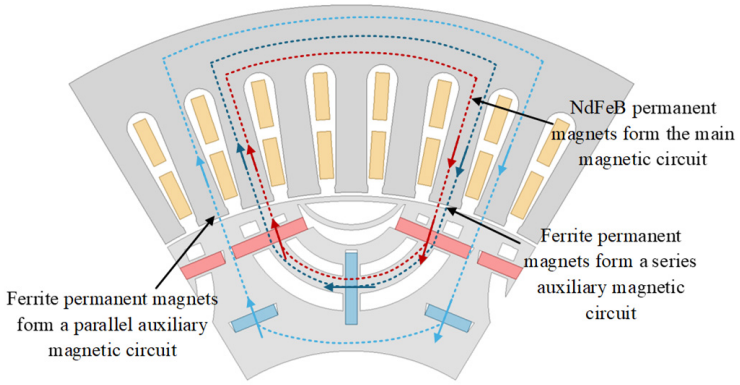

FIGURE 3. Diagram of the HPM-VLFM magnetic circuit and the magnetization directions of its permanent magnets.

the output torque of the VLFM, ferrite permanent magnets are added in series and parallel to strengthen the main magnetic circuit of the VLFM, resulting in the HPM-VLFM. Additionally, since the HPM-VLFM features spoke-type ferrite permanent magnets on the q-axis, this further reduces the q-axis inductance and improves the HPM-VLFM's reverse convexity ratio. To more intuitively demonstrate the effect of adding ferrite permanent magnets on the HPM-VLFM, a schematic diagram of the HPM-VLFM magnetic circuit and the magnetization directions of each permanent magnet were drawn, as shown in Figure 3. In summary, through the aforementioned series of innovative designs, the target motor, HPM-VLFM, was ultimately achieved.

2.2. Equivalent Magnetic Circuit Analysis of Electric Motors

The excitation source of the HPM-VLFM consists of a series-parallel circuit formed by neodymium-iron-boron permanent magnets and ferrite permanent magnets. Additionally, the rotor is designed with a magnetic barrier to introduce a leakage flux path and reduce the cross-axis inductance. To more clearly illustrate the advantages of the HPM-VLFM, this paper establishes equivalent magnetic circuits for the CPMSM, VLFM, and HPM-VLFM for analysis and comparison. Each main magnetic path consists of a magnetic potential source, a magnetic barrier with equivalent magnetic resistance, and an air gap, thereby enabling simplified modeling of the magnetic circuit, as shown in Figure 4.

Variable-leakage-flux motors actively regulate their internal magnetic circuits through controllable leakage flux paths. The variation in their inductance directly reflects the regulatory effect of the leakage flux paths on the magnetic circuit, and directly determines the weak-field speed control capability and the proportion of reluctance torque. Therefore, based on Figure 4, this paper calculates and analyzes the *dq*-axis inductance and flux characteristics of equivalent magnetic circuits for different motors to illustrate the advantages of the HPM-VLFM.

As shown in Figure 4(a), for a CPMSM, the *dq*-axis inductance is expressed as follows:

$$\begin{cases} L_d = \frac{N^2}{R_s+R_g+R_{pm}+R_r} \\ L_q = \frac{N^2}{R_s+R_g+R_r} \end{cases} \tag{1}$$

Here, L_d and L_q represent the *dq*-axis inductances, respectively; R_s is the stator equivalent magnetic resistance; R_g is the air gap equivalent magnetic resistance; R_{pm} is the permanent magnet equivalent magnetic resistance; and R_r is the rotor equivalent magnetic resistance. The electromagnetic torque of a PMSM typically consists of two components: permanent magnet torque and reluctance torque. Since the inductance L_d of a CPMSM is less than L_q, its reluctance torque is reduced, thereby decreasing the electromagnetic torque. The formula for calculating the electromagnetic torque is as follows:

$$T_e = \frac{3p}{2}\left[\psi_m i_q + (L_d - L_q) i_d i_q\right] \tag{2}$$

As shown in Figure 4(b), compared to the CPMSM, the VLFM incorporates two additional leakage flux paths and two magnetic bridges. In this configuration, the VLFM includes a d-axis leakage flux resistance (R_{bd}) in parallel with the d-axis magnetic circuit and a q-axis leakage flux resistance (R_{bq}) in series with the q-axis magnetic circuit. Consequently, the d-axis inductance L_d of the VLFM decreases, while the q-axis inductance L_q increases. Assuming that magnetic saturation and the rotor's angular position are neglected, L_d and L_q of the VLFM can be expressed as:

$$\begin{cases} L_d = \frac{N^2}{R_s+R_g+(R_{pm}+R_r)\|R_{bd}} \\ L_q = \frac{N^2}{R_s+R_g+R_r+R_{bq}} \end{cases} \tag{3}$$

When the VLFM operates at high speeds, the q-axis current increases. Due to the saturation of the magnetic barrier, the magnetic resistance increases significantly, and the inductance decreases, resulting in $L_d > L_q$, which increases the torque to some extent. At the same time, the increase in magnetic resistance also increases the magnetic flux to some extent. The permanent magnet flux and armature flux of the VLFM can be expressed as follows:

$$\begin{bmatrix} \phi_s \\ \phi_{pm} \end{bmatrix} = \frac{L_d}{N^2} \cdot A(R) \begin{bmatrix} F_d \\ F_{pm} \end{bmatrix} \tag{4}$$

$$\phi_{bd} = \phi_{pm} - \phi_s \tag{5}$$

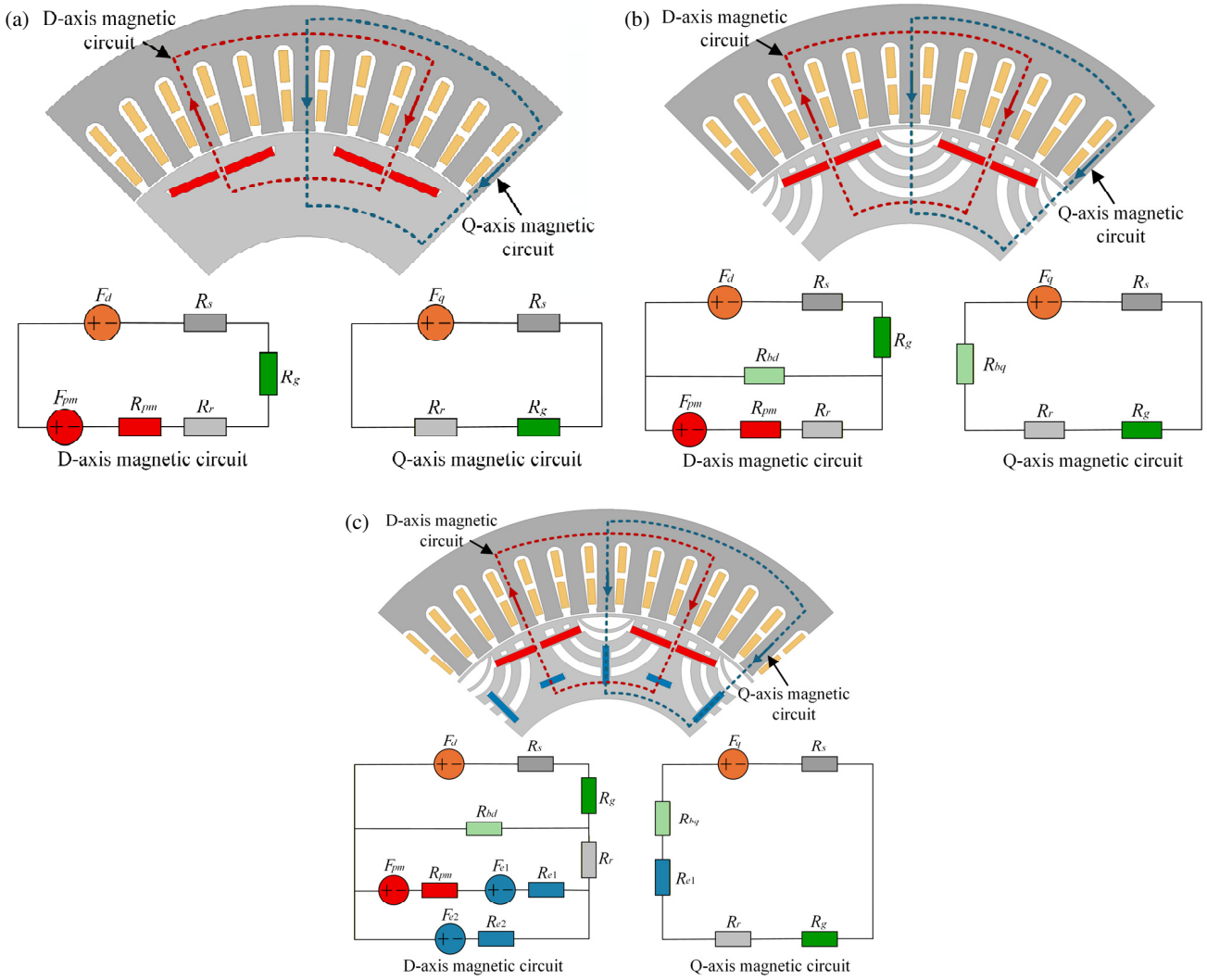

FIGURE 4. Equivalent circuit analysis: (a) CPMSM. (b) VLFM. (c) HPM-VLFM.

where,

$$A(R) = \begin{bmatrix} 1 & -\frac{R_{bd}}{R_{pm}+R_r+R_{bd}} \\ \frac{R_{bd}}{R_{pm}+R_r+R_{bd}} & -\frac{R_s+R_g+R_{bd}}{R_{pm}+R_r+R_{bd}} \end{bmatrix} \tag{6}$$

Compared to CPMSMs, the leakage flux (Φ_{bd}) of VLFMs is related to the leakage magnetic resistance (R_{bd}); therefore, by appropriately designing the leakage magnetic resistance to control the leakage flux, the air gap flux can be regulated. To further increase motor torque, the HPM-VLFM employs a series-parallel arrangement of ferrite permanent magnets to alter the *dq*-axis inductance and flux. The L_d and L_q of the HPM-VLFM can be expressed as follows:

$$\begin{cases} L_d = \frac{N^2}{R_s+R_g+[(R_{pm}+R_{e1})\|R_{e2}+R_r]\|R_{bd}} \\ L_q = \frac{N^2}{R_s+R_g+R_r+R_{bq}+R_{e1}} \end{cases} \tag{7}$$

Here, R_{e1} represents the equivalent magnetic resistance of the series-connected ferrite permanent magnets, and R_{e2} represents the equivalent magnetic resistance of the parallel-connected ferrite permanent magnets.

Compared to the VLFM, using Thevenin's equivalence theorem, the series-parallel permanent magnets in the HPM-VLFM can be equivalent to a single series magnetic resistance with a magnetic field:

$$\begin{cases} F_{eq} = \frac{(F_{pm}-F_{e1})R_{e2}+F_{e2}(R_{pm}+R_{e1})}{R_{pm}+R_{e1}+R_{e2}} \\ R_{eq} = (R_{pm}+R_{e1})\|R_{e2} \end{cases} \tag{8}$$

Here, F_{e1} represents the equivalent magnetic flux density of the series-connected ferrite permanent magnets, and F_{e2} represents the equivalent magnetic flux density of the parallel-connected ferrite permanent magnets. After applying the Thevenin transformation, the equivalent magnetic circuit resembles the VLFM model. Based on this, in addition to adjusting the inductance and magnetic flux by varying the size of the magnetic barrier, the precise design of an enhanced-output-torque variable-leakage-flux motor can also be achieved by varying the size of the ferrite permanent magnets. The key design parameters for CPMSM, VLFM, and HPM-VLFM are shown in Table 1.

TABLE 1. Main dimensions and parameters of CPMSM, VLFM, and HPM-VLFM.

Items	CPMSM	VLFM	HPM-VLFM
Rated Current (A)	30	30	30
Air-gap length (mm)	0.6	0.6	0.6
Rated speed (rpm)	1000	1000	1000
Out diameter of stator (mm)	190	190	190
Out diameter of rotor (mm)	123.8	123.8	123.8
Effective laminate length (mm)	100	100	100
Number of slots/poles	48/8	48/8	48/8
Use of NdFeB per pole/(mm^3)	6052.5	6052.5	6052.5
Use of Ferrite per pole/(mm^3)	0	0	4082

3. MULTI-OBJECTIVE OPTIMIZATION

For the proposed hybrid permanent magnet synchronous motor with variable leakage flux (HPM-VLFM) using a series-parallel permanent magnet configuration, the design of the stator and windings is primarily based on conventional bar-type permanent magnet synchronous motors (Table 1) and classic design formulas for permanent magnet synchronous motors. To better analyze the variable leakage flux characteristics of the HPM-VLFM, modeling results of the equivalent magnetic circuit indicate that, to achieve variable leakage flux, the rotor magnetic barrier and permanent magnet dimensions must first be optimized to obtain optimal performance.

Figure 5 shows the main parameters of the HPM-VLFM, and the specific design variables and their value ranges are listed in Table 2. Furthermore, considering that the HPM-VLFM should possess high torque, stability, and a wide speed regulation range, the average torque (T_{avg}), torque ripple (T_{riple}), and Reverse-salient ratio (L_d/L_q) are set as optimization objectives.

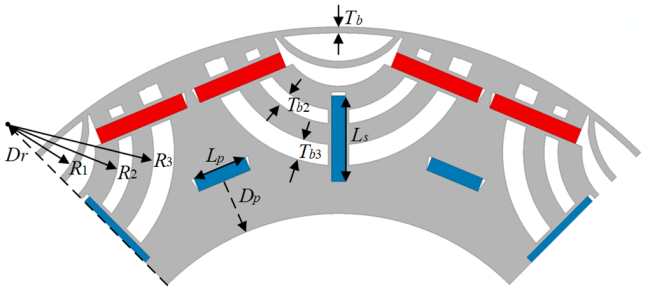

FIGURE 5. Key specifications of the HPM-VLFM.

Based on the parameterized model of HPM-VLFM shown in Figure 5, this paper uses sensitivity analysis to examine the extent to which each variable influences the optimization objective. The sensitivity indices are shown in Figure 6; these values indicate whether the influence of each variable on the optimization objective is positively or negatively correlated.

As shown in Figure 6, R_1 has the greatest influence on average torque and torque ripple, while T_b has the greatest influence on the back-convexity ratio. The results indicate that the degree of influence of each variable on the optimization objectives varies significantly. Therefore, this paper selects high-sensitivity parameters for response surface analysis. The response surfaces for average torque, torque ripple, and Back-Reverse-salient ratio of the HPM-VLFM are shown in Figure 8. By examining the response surfaces, the relationships between the parameters and the response variables can be determined, and the response variables can be predicted within specific ranges. Finally, an evolutionary algorithm (EA) was employed to perform multi-objective optimization design, and the optimal solution was obtained based on the constraints, as shown in Figure 7.

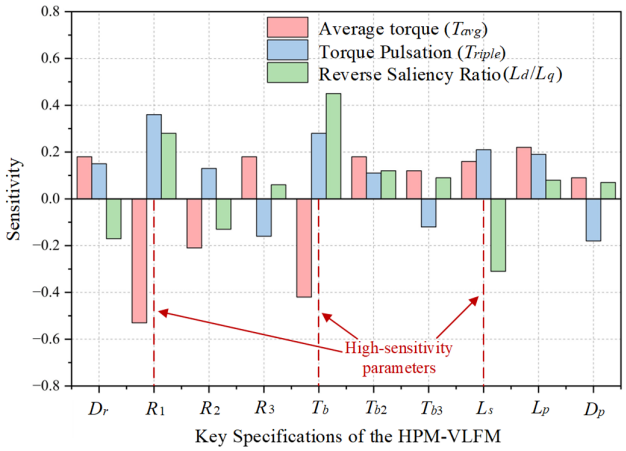

FIGURE 6. Sensitivity analysis results for HPM-VLFM.

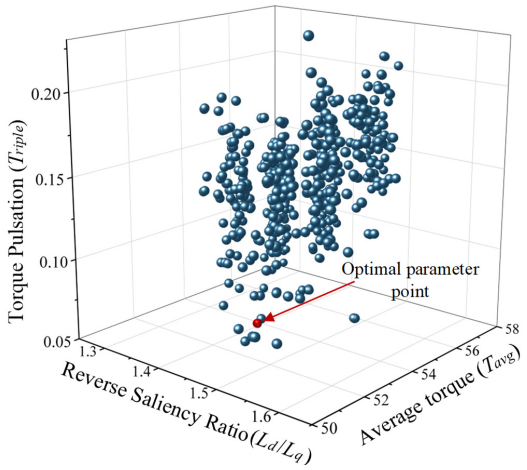

FIGURE 7. Optimal solution for HPM-VLFM.

4. ANALYSIS AND COMPARISON OF ELECTROMAGNETIC PROPERTIES

4.1. Analysis of Variable Leakage Flux Characteristics

Figure 9 shows the magnetic field distributions of the CPMSM, VLFM, and HPM-VLFM under no-load and loaded conditions, respectively. During no-load operation, all three motors exhibit significant stray magnetic fields. During loaded operation, when an inter-axis current (i_q) is applied, most of the magnetic flux lines in the VLFM and HPM-VLFM pass through the stator and are attenuated via the stray magnetic path, thereby

TABLE 2. Design variables of the HPM-VLFM and their ranges.

Parameters	Introduction	Value range
D_r	Distance between the center of the magnetic barrier and the inner diameter of the stator	[31–35]
R_1	The distance from the first magnetic barrier to the center of the circle	[10–12]
R_2	The distance from the second magnetic barrier to the center of the circle	[16–19]
R_3	The distance from the third magnetic barrier to the center of the circle	[21–25]
T_b	Magnetic bridge thickness	[4–5]
T_{b2}	Thickness of the second magnetic barrier	[1–2]
T_{b3}	Thickness of the third magnetic barrier	[2–4]
L_s	Length of a series-connected permanent magnet	[11–13]
L_p	Length of a parallel-connected permanent magnet	[6–9]
D_p	Distance between the parallel-connected permanent magnets and the stator inner diameter	[7–10]

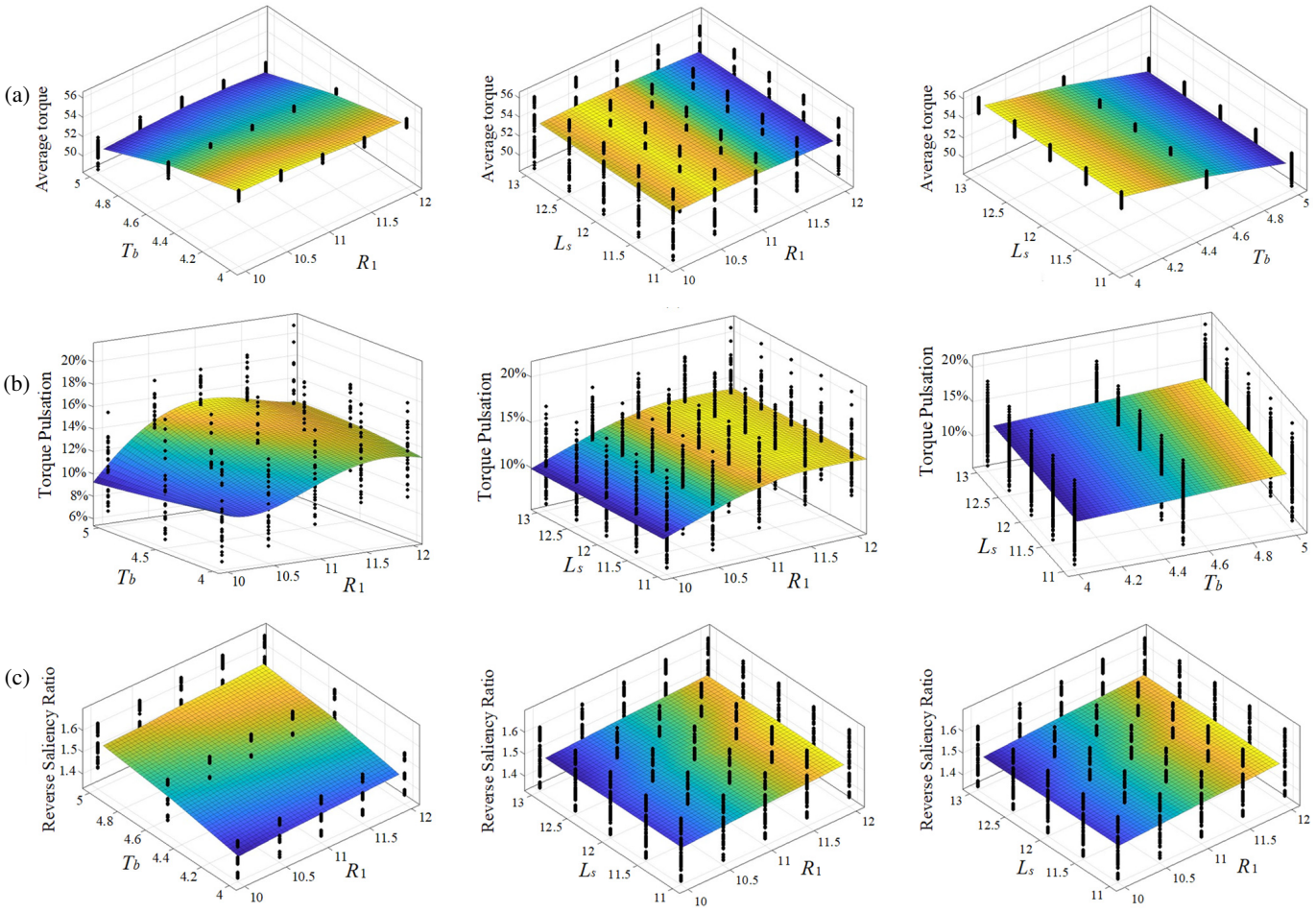

FIGURE 8. High-sensitivity parameter response surface analysis: (a) Average torque response surface analysis; (b) Torque ripple response surface analysis; (c) Back-reverse-salient ratio response surface analysis.

providing superior weak-field capability and generating greater torque. A comparison of Figures 9(b) and 9(c) shows that the magnetic flux density is significantly enhanced due to the addition of series-parallel ferrite permanent magnets [18].

Furthermore, to conduct a more in-depth analysis of the variable leakage flux characteristics of the VLFM and HPM-VLFM, this paper investigates the variation of the axial magnetic flux with the q-axis current, as shown in Figure 10. As can

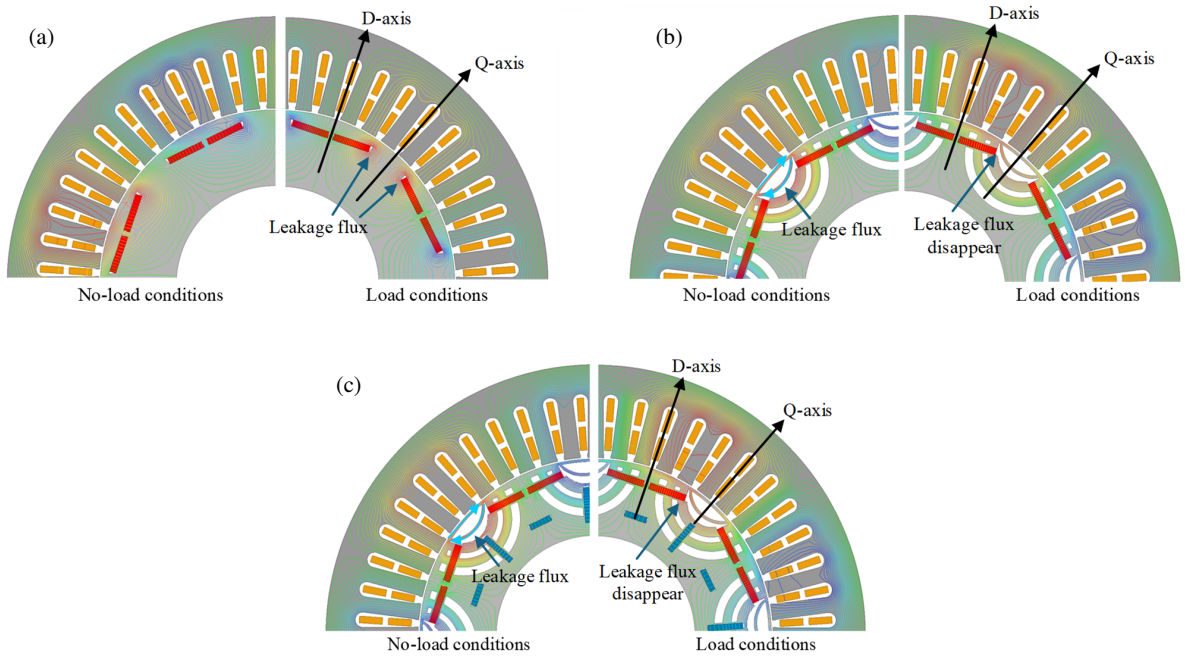

FIGURE 9. Magnetic field distribution under no-load and loaded conditions: (a) CPMSM. (b) VLFM. (c) HPM-VLFM.

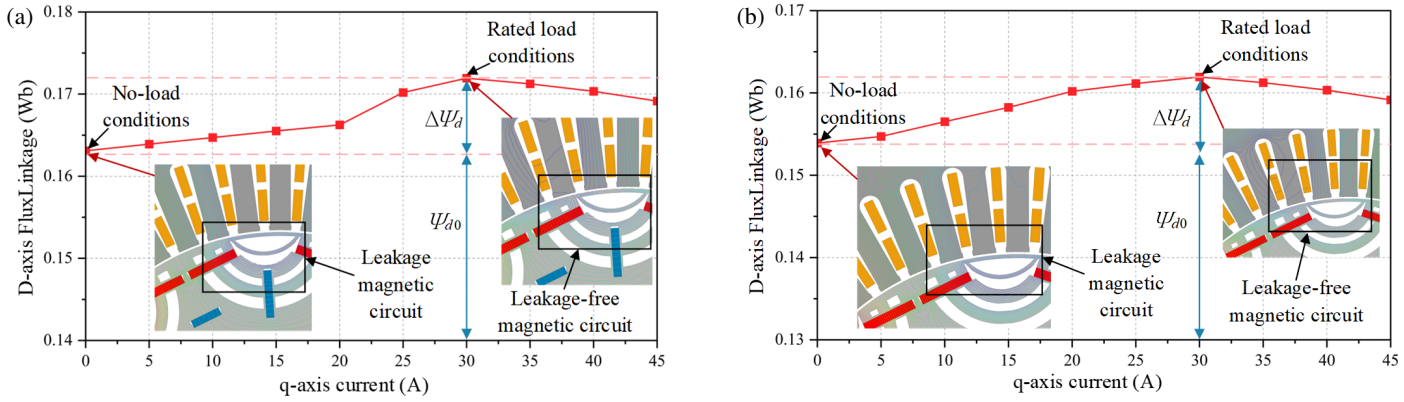

FIGURE 10. Analysis of variable leakage flux characteristics: (a) VLFM. (b) HPM-VLFM.

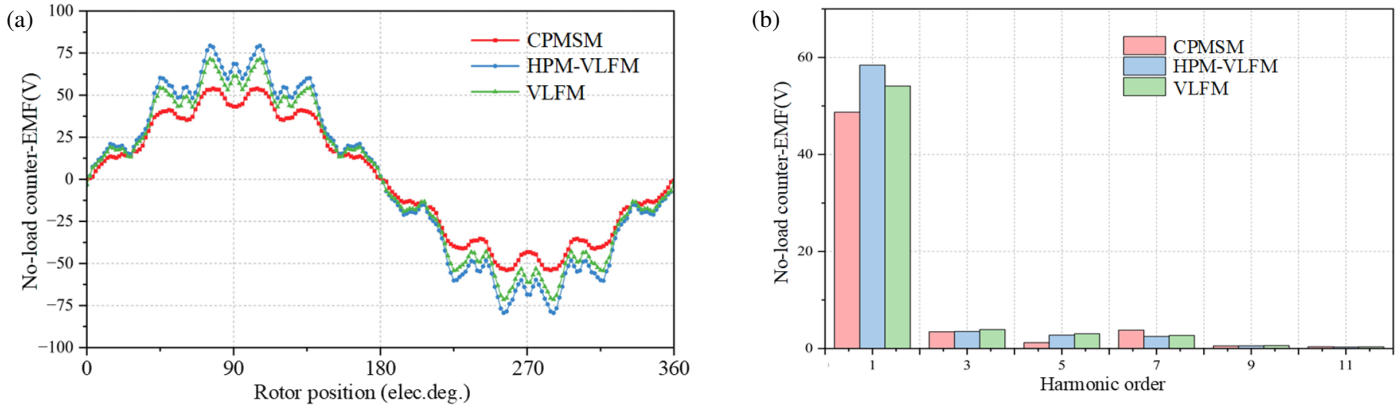

FIGURE 11. No-load back EMF: (a) Back EMF at different rotor positions. (b) Fourier decomposition.

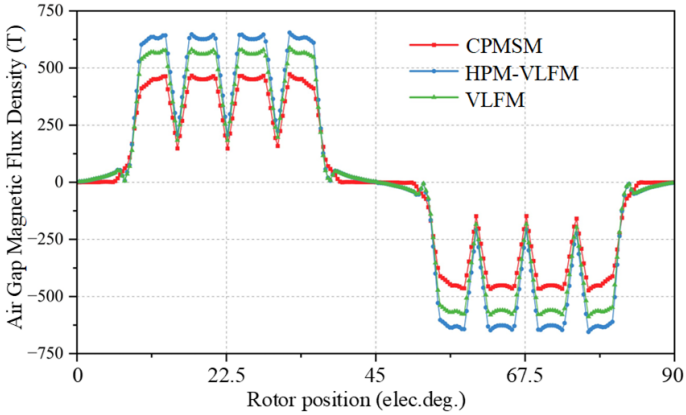

FIGURE 12. No-load air gap magnetic flux density.

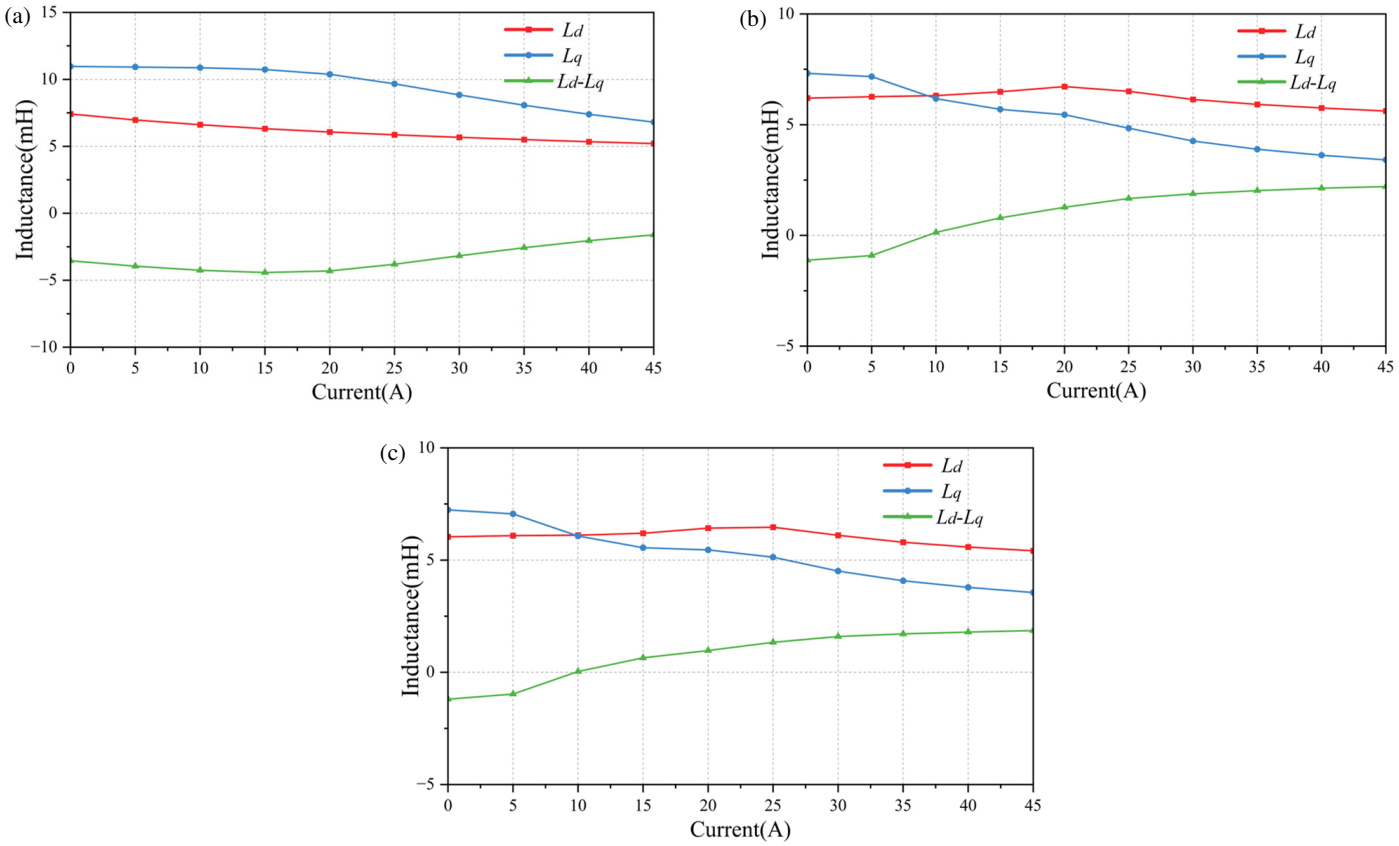

FIGURE 13. Analysis of inductance characteristics: (a) CPMSM. (b) VLFM. (c) HPM-VLFM.

be seen from the figure, when $i_q = 0$, the magnetic flux lines of the VLFM and HPM-VLFM pass through the leakage flux path, and the axial magnetic flux is minimal. As i_q increases, the magnetic flux along the vertical axis continues to rise, reaching a peak when the current reaches 30 A. When $i_q > 30$ A, the motor's leakage flux gradually approaches saturation; therefore, as i_q increases, the magnetic flux along the vertical axis decreases.

4.2. No-Load Characteristics Analysis

Figure 11(a) shows the no-load back-EMF waveforms of the three motor types. It can be seen that, due to its variable leakage flux design, the no-load back-EMF amplitude of the VLFM is higher than that of conventional motors. Furthermore, due to the ferrite permanent magnet design of the HPM-VLFM, its no-load back-EMF amplitude is higher than that of the VLFM. A Fourier transform was performed on the no-load back-EMF to conduct a harmonic analysis, with the results shown in Figure 11(b). The results indicate that the total harmonic distortion (THD) value for the CPMSM, HPM-VLFM, and VLFM are 11.87%, 8.81%, and 10.47%, respectively, demonstrating that the no-load back-EMF waveform of the new motor is more sinusoidal. The air gap is a core component for energy conversion in motors, making its analysis crucial. Figure 12 com-

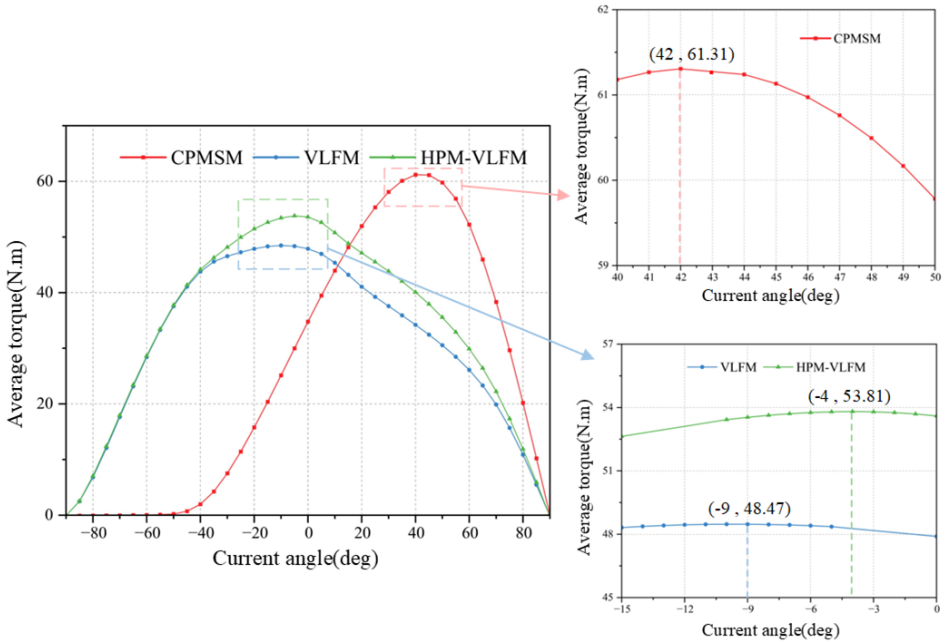

FIGURE 14. Analysis of average output torque and current-angle relationship.

pares the air gap magnetic flux density of the CPMSM, VLFM, and HPM-VLFM, showing that the HPM-VLFM has the highest peak air gap magnetic flux density.

4.3. Inductance Analysis

Inductance plays a critical role in the motor's output torque, speed control range, and flux decay characteristics. By implementing a differentiated topological design for the L_d and L_q of a PMSM, it is possible to effectively optimize the motor's torque density, operating efficiency, and high-speed performance; therefore, it is necessary to analyze the motor's inductance.

Figure 13 shows the inductance characteristics of three motors under different current conditions. As shown in Figure 13(a), the CPMSM exhibits an $L_d < L_q$ characteristic, and as the current increases, the difference between L_d and L_q gradually decreases due to magnetic saturation. Figures 13(b) and (c) show that the VLFM and HPM-VLFM achieve an $L_d > L_q$ characteristic; simultaneously, due to magnetic saturation at the magnetic bridge, the difference between L_d and L_q gradually decreases. Therefore, by adding a magnetic bridge and magnetic barrier structures, an $L_d > L_q$ inductance characteristic can be achieved.

4.4. Torque-Efficiency Analysis

According to Equation (2), torque depends not only on the applied current but also on the *dq* axis and inductance. Therefore, when the CPMSM reaches maximum torque, its current angle is positive; when the VLFM and HPM-VLFM reach maximum torque, their current angles are negative. The relationship between average output torque and current angle is shown in Figure 14. As shown in the figure, when the current angle is 42 degrees, the CPMSM's torque reaches a maximum of 61.31 N·m;

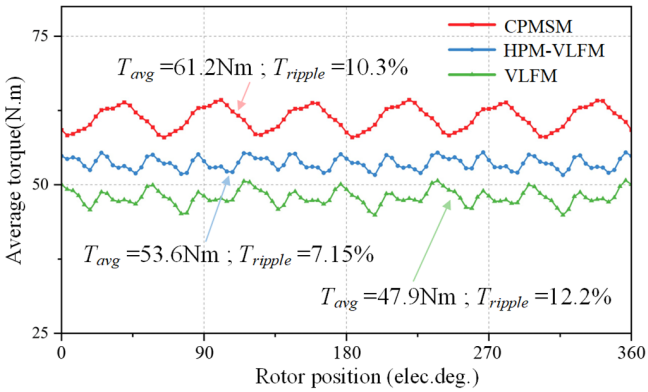

FIGURE 15. Analysis of inductance characteristics: CPMSM, VLFM, HPM-VLFM.

when the current angles are $-9°$ and $-4°$, respectively, the torque of the VLFM and HPM-VLFM reaches maximum values of 48.47 N·m and 53.81 N·m, respectively. Therefore, because variable-leakage-flux motors incorporate magnetic barriers at the rotor, resulting in lower magnetic flux density, the output torque capacity of the VLFM and HPM-VLFM is lower than that of the CPMSM.

In addition, torque ripple is a key performance metric in motor design. Figure 15 illustrates the torque ripple characteristics of the three motor types. As shown in the figure, due to the effect of the magnetic barrier, the torque ripple of the VLFM and HPM-VLFM is lower than that of the CPMSM. Specifically, the torque ripple of the CPMSM is 10.3%, that of the VLFM is 12.2%, and that of the HPM-VLFM is 7.15%.

This paper employs a maximum torque-to-current ratio (MTPA) control strategy to generate efficiency MAP plots for the CPMSM, VLFM, and HPM-VLFM, as shown in Figure 16.

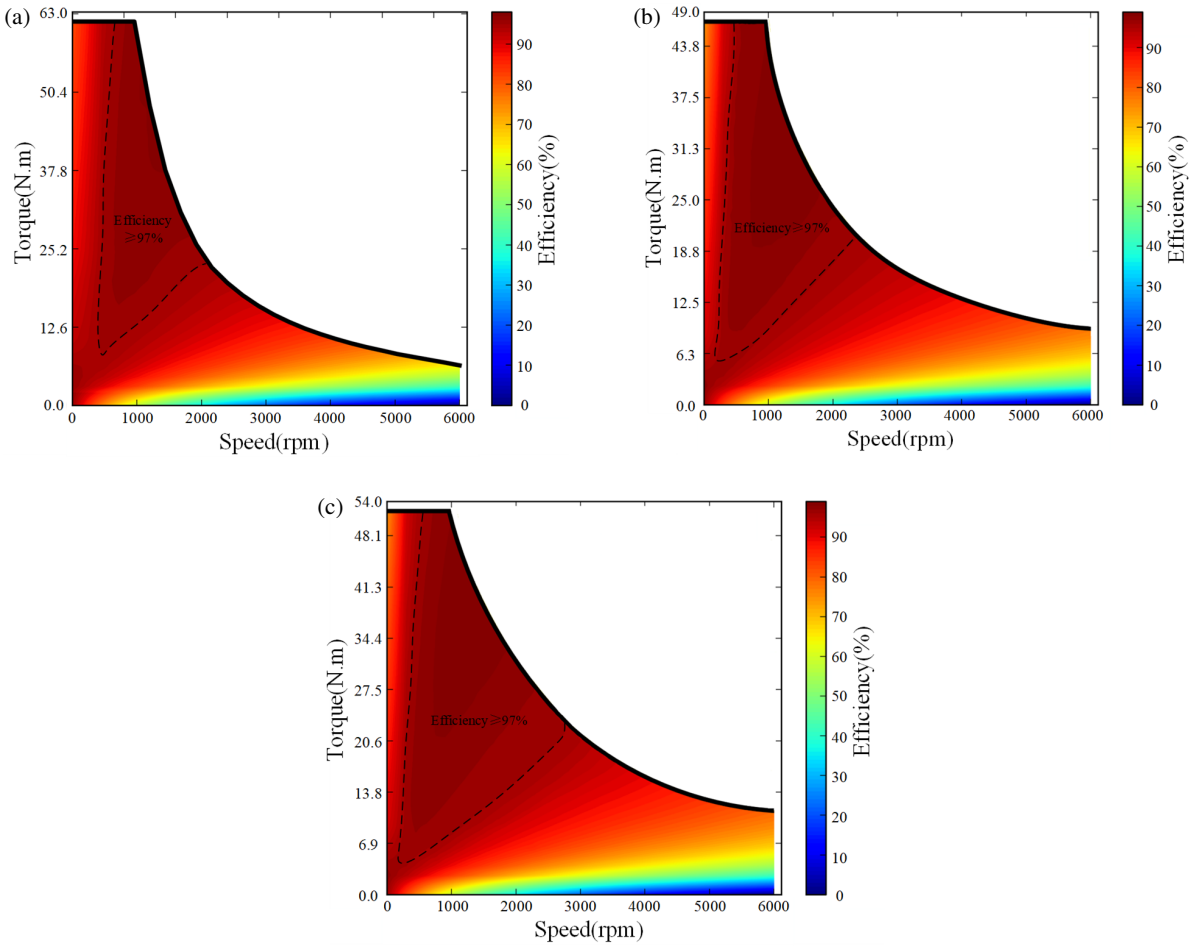

FIGURE 16. Efficiency MAP: (a) CPMSM. (b) VLFM. (c) HPM-VLFM.

As shown in the figure, due to the variable leakage flux design, the speed control range of the VLFM and HPM-VLFM is wider than that of the CPMSM. In the 0–2500 r/min speed range, the high-efficiency region of the VLFM and HPM-VLFM is broader than that of the CVTSM. Comparing Figures 16(b) and (c) reveals that, compared to the VLFM, the HPM-VLFM has a wider speed range and higher efficiency. This demonstrates that the addition of series-parallel permanent magnets in the HPM-VLFM enhances the magnetic circuit.

5. CONCLUSION

To address the shortcomings of conventional permanent magnet synchronous motors (CPMSMs), such as the inability to adjust the permanent magnet field and a narrow speed control range, this paper proposes a variable-flux permanent magnet motor (VLFM) utilizing strip-shaped neodymium-iron-boron permanent magnets, based on the advantages of variable-flux-magnetism. Furthermore, to enhance the output torque of the VLFM, a hybrid permanent magnet variable-flux permanent magnet synchronous motor (HPM-VLFM) is developed by designing ferrite permanent magnets in series-parallel magnetic circuits. The proposed motor is evaluated using finite element analysis (FEA), leading to the following conclusions:

(1) By performing equivalent magnetic circuit analysis on different motors, this paper elucidates the basic principles of variable leakage flux as well as the principles of magnetic circuit enhancement using series-parallel permanent magnets.

(2) Through the rational design of magnetic barriers and analysis of variable leakage flux characteristics, the VLFM and HPM-VLFM achieve magnetic field weakening via leakage flux paths, demonstrating superior weak-field performance.

(3) Torque-efficiency analysis shows that when the VLFM and HPM-VLFM reach maximum torque, their current angle is negative, consistent with the principles of inductance and magnetic circuit analysis. Additionally, due to the variable leakage flux and the design of series-parallel ferrite permanent magnets, the HPM-VLFM offers a wider speed control range and higher efficiency.

REFERENCES

[1] Zhu, X., J. Huang, L. Quan, Z. Xiang, and B. Shi, "Comprehensive sensitivity analysis and multiobjective optimization research of permanent magnet flux-intensifying motors," *IEEE Transactions on Industrial Electronics*, Vol. 66, No. 4, 2613–2627, Apr. 2019.

[2] Tosun, O., N. F. O. Serteller, U. Demir, O. Akar, and V. Esen, "Multi-objective design improvement of a double-stator single-

rotor axial flux brushless DC motor with a focus on efficiency," *Elektronika ir Elektrotechnika*, Vol. 31, No. 5, 17–25, 2025.

[3] Zhou, X., X. Zhu, W. Wu, Z. Xiang, Y. Liu, and L. Quan, "Multi-objective optimization design of variable-saliency-ratio PM motor considering driving cycles," *IEEE Transactions on Industrial Electronics*, Vol. 68, No. 8, 6516–6526, Aug. 2021.

[4] Liu, X., H. Hu, Q. Jia, Z. Liu, and Z. Zhu, "Lower cost variable-leakage-flux reverse-salient-pole permanent magnet motor by reducing rare-earth permanent magnet usage," *Progress In Electromagnetics Research C*, Vol. 166, 57–67, 2026.

[5] Kashif, M. and B. Singh, "Design of a new spoke-PMSM with multiple flux barriers considering flux-intensifying effect for SWPS," in *2021 IEEE 12th Energy Conversion Congress & Exposition — Asia (ECCE-Asia)*, 521–525, Singapore, 2021.

[6] Yang, H., H. Lin, and Z. Q. Zhu, "Recent advances in variable flux memory machines for traction applications: A review," *CES Transactions on Electrical Machines and Systems*, Vol. 2, No. 1, 34–50, Mar. 2018.

[7] Hu, Z., X. Liu, Z. Liu, Z. Huang, W. Hu, and Z. Shi, "Design and analysis of wide speed-regulated reverse salient-pole variable leakage flux interior permanent magnet machine," in *2023 IEEE 6th Student Conference on Electric Machines and Systems (SCEMS)*, 1–6, Huzhou, China, 2023.

[8] Zhu, W., X. Zhu, and Z. Xiang, "Research on power factor improvement of a variable-leakage-flux PM motor based on regulated-flux-barrier topology," *IEEE Transactions on Magnetics*, Vol. 60, No. 9, 1–6, Sep. 2024.

[9] Abdel-Mageed, B. S., A. M. Aljehaimi, and P. Pillay, "Analysis of design topologies for variable flux permanent magnet motors," *IEEE Transactions on Industry Applications*, Vol. 62, No. 1, 939–955, Jan.–Feb. 2026.

[10] Abdel-Mageed, B. S., A. M. Aljehaimi, and P. Pillay, "Modeling and remedies for rare-earth permanent magnet demagnetization effects in hybrid permanent magnet variable flux motors," *IEEE Transactions on Energy Conversion*, Vol. 40, No. 1, 490–504, Mar. 2025.

[11] Xu, H., J. Li, J. Chen, Y. Lu, and M. Ge, "Analysis of a hybrid permanent magnet variable-flux machine for electric vehicle tractions considering magnetizing and demagnetizing current," *IEEE Transactions on Industry Applications*, Vol. 57, No. 6, 5983–5992, Nov.–Dec. 2021.

[12] Qiao, G., Y. Liu, M. Wang, F. Liu, and P. Zheng, "Study of a high-efficiency series-parallel-connected hybrid-PM variable-flux permanent magnet synchronous machine," *IEEE Transactions on Magnetics*, Vol. 58, No. 2, 1–7, Feb. 2022.

[13] Barman, D. and P. Pillay, "Effect of skewing in a variable flux interior permanent magnet synchronous machine," *IEEE Transactions on Industry Applications*, Vol. 56, No. 6, 6399–6410, Nov.-Dec. 2020.

[14] Zhao, W., Z. Yang, Y. Liu, and X. Wang, "Analysis of a novel surface-mounted permanent magnet motor with hybrid magnets for low cost and low torque pulsation," *IEEE Transactions on Magnetics*, Vol. 57, No. 6, 1–4, Jun. 2021.

[15] Du, Z. S. and T. A. Lipo, "Cost-effective high torque density bi-magnet machines utilizing rare earth and ferrite permanent magnets," *IEEE Transactions on Energy Conversion*, Vol. 35, No. 3, 1577–1584, Sep. 2020.

[16] Fan, D., X. Zhu, L. Quan, P. Han, Z. Xiang, and J. Wu, "Driving cycle design optimization of less-rare-earth PM motor using dimension reduction method," *IEEE Transactions on Energy Conversion*, Vol. 38, No. 3, 1614–1625, Sep. 2023.

[17] Chen, Y., T. Cai, X. Zhu, D. Fan, and Q. Wang, "Analysis and design of a new type of less-rare-earth hybrid-magnet motor with different rotor topologies," *IEEE Transactions on Applied Superconductivity*, Vol. 30, No. 4, 1–6, Jun. 2020.

[18] Chen, Y., T. Cai, X. Zhu, and Y. Ding, "Optimization of a new asymmetric-hybrid-PM machine with high torque density and low torque ripple considering the difference of magnetic materials," *IEEE Transactions on Magnetics*, Vol. 58, No. 2, 1–5, Feb. 2022.